Acta Materialia 115 (2016) 115–122

Contents lists available at ScienceDirect

Acta Materialia

journal homepage: www.elsevier.com/locate/actamat

Full length article

Bubble formation and lattice parameter changes resulting from He irradiation of defect-fluorite $Gd_2Zr_2O_7$

Caitlin A. Taylor [a, *], Maulik K. Patel [a], Jeffery A. Aguiar [b, c], Yanwen Zhang [d, a], Miguel L. Crespillo [a], Juan Wen [e, f], Haizhou Xue [a], Yongqiang Wang [f], William J. Weber [a, d]

[a] Department of Materials Science and Engineering, The University of Tennessee, Knoxville, TN 37996, USA
[b] Fuel Performance and Design Department, Idaho National Laboratory, Idaho Falls, ID 83415-6188, USA
[c] Material Science Center, National Renewable Energy Laboratory, Golden, CO 80220, USA
[d] Materials Science and Technology Division, Oak Ridge National Laboratory, Oak Ridge, TN 37831, USA
[e] School of Nuclear Science and Technology, Lanzhou University, Lanzhou, Gansu 730000, China
[f] Materials Science and Technology Division, Los Alamos National Laboratory, Los Alamos, NM 87545, USA

ARTICLE INFO

Article history:
Received 4 May 2016
Received in revised form
24 May 2016
Accepted 27 May 2016
Available online 6 June 2016

Keywords:
Pyrochlore
Helium bubble
Radiation damage
Nuclear waste
Lattice swelling

ABSTRACT

Pyrochlores have long been considered as potential candidates for advanced ceramic waste-forms for the immobilization of radioactive waste nuclides. This work provides evidence that $Gd_2Zr_2O_7$, often considered the most radiation tolerant pyrochlore, could be susceptible to radiation damage in the form of bubble nucleation at the highest He doses expected over geological time. Ion irradiations were utilized to experimentally simulate the radiation damage and He accumulation produced by α-decay. Samples were pre-damaged using 7 MeV Au^{3+} to induce the pyrochlore to defect-fluorite phase transformation, which would occur due to α-recoil damage within several hundred years of storage in a $Gd_2Zr_2O_7$ waste-form. These samples were then implanted to various He concentrations in order to study the long-term effects of He accumulation. Helium bubbles 1–3 nm in diameter were observed in TEM at a concentration of 4.6 at.% He. Some bubbles remained isolated, while others formed chains 10–30 nm in length parallel to the surface. GIXRD measurements showed lattice swelling after irradiating pristine $Gd_2Zr_2O_7$ with 7 MeV Au^{3+} to a fluence of 2.2×10^{15} Au/cm^2. An increase in lattice swelling was also measured after 2.2×10^{15} Au/cm^2 + 2×10^{15} He/cm^2 and 2.2×10^{15} Au/cm^2 + 2×10^{16} He/cm^2. A decrease in lattice swelling was measured after irradiation with 2.2×10^{15} Au/cm^2 + 2×10^{17} He/cm^2, the fluence where bubbles and bubble chains were observed in TEM. Bubble chains are thought to form in order to reduce lattice strain normal to the surface, which is produced by the Au and He irradiation damage.

1. Introduction

Ceramics considered for radioactive waste immobilization generally have complex crystal structures to facilitate the accommodation of various uniquely sized actinides at crystallographic lattice sites. Direct incorporation of actinides at lattice sites allows crystalline matrices, including pyrochlore, to achieve higher chemical durability than traditional glass host matrices [1,2]. In addition, some difficult "legacy" waste streams from past military or civil nuclear programs cannot undergo vitrification using current technology [3]. Pyrochlores, with structural formula $A_2B_2O_7$ (space group *Fd*-3*m* (No. 227)), where A- and B- sites contain metal cations, have long been considered a potential actinide immobilization host phase [4] because of their ability to accommodate various minor actinides at the A- and B- sites.

Pyrochlore differs from the fluorite structure in that there are two cation sites and one-eighth of the anions are absent. The cations and oxygen vacancies are ordered, with A-site cations occupying the *16d* site and B-site cations occupying the *16c* site. Oxygen anions occupy the *48f* and *8a* positions, with oxygen vacancies occupying the *8b* sites. The position of oxygen anions in the *48f* position shifts because the oxygen positional parameter *x* changes to incorporate various cation sizes [5]. Under irradiation, $Gd_2Zr_2O_7$ undergoes an order-disorder transformation from pyrochlore to defect-fluorite at ~0.4 dpa [6]. In a defect-fluorite (space group *Fm*-3*m* (No. 225)), the cations are randomly distributed on the fluorite

* Corresponding author.
E-mail address: ctayl105@vols.utk.edu (C.A. Taylor).

http://dx.doi.org/10.1016/j.actamat.2016.05.045
1359-6454/

cation sublattice (*4a* site) while the oxygen anions (7 per cell) and oxygen anion vacancies (1 per cell) are randomly distributed on the fluorite anion sublattice (*8c* site) [7]. Fig. 1 illustrates the differences between the pyrochlore and defect-fluorite structures.

Much of the previous radiation damage work involving pyrochlores has focused on either predicting the radiation stability based on the cation radius ratio (r_A/r_B) [7], or on identifying the total damage dose required to induce amorphization or the pyrochlore to defect-fluorite transformation [2,4]. Understanding phase transformations is of critical importance for identifying prospective waste-form materials because structural changes often result in altered chemical properties or responses to irradiation damage. For example, amorphization increased the leach rate of Cm and Gd in the pyrochlore $Gd_{1.935}Cm_{0.065}TiZrO_7$ which was placed in water for 14 days at 90 °C [8]. In general, pyrochlores with similar cation radii more easily form antisite defects, which allows the structure to easily transform to the more stable defect-fluorite structure under irradiation. Pyrochlores with dissimilar cation radii cannot easily form the defect-fluorite structure [7], and the pyrochlore structure collapses under irradiation, leading to amorphization. Amorphization has been observed in the widely studied titanate pyrochlores at various doses [9] and many become fully amorphous near 0.2 dpa [4]. Zirconate pyrochlores, which have similar A- and B- site cation radii, easily transform to defect-fluorite under irradiation [7]. $Gd_2Zr_2O_7$ (GZO), often considered the most radiation tolerant pyrochlore, is resistant to amorphization at cryogenic temperatures, even at 100 dpa [10], making the structure a desirable host for radionuclide immobilization.

Depending on actinide content, waste-form matrices will undergo varying amounts of displacement damage due to low energy (typically ≈100 keV) recoil atoms (daughter nuclei) produced during α-decay processes from plutonium and other minor actinides for hundreds of thousands of years [11]. Though damage in a real waste-form depends on waste loading, displacement damage will, for example, transform GZO to the defect-fluorite phase within one hundred years of storage in a waste-form containing 5 wt% minor actinides (Fig. 2). Beyond this point, He atoms will continue to accumulate due to α-decay, causing the host matrix to swell or reach a critical He concentration sufficient for bubble nucleation. Helium accumulation in a real waste-form could create mechanical stresses that lead to cracking, creating a path for ground water to penetrate the waste-form, thereby providing a mechanism for contamination and leaching radioactive material. In this work, we attempt to simulate the combined effects of α-recoil damage and He accumulation by pre-damaging GZO samples prior to He implantation. The pre-damage step serves to (1) simulate α-recoil damage that would occur prior to significant He accumulation, and (2) transform GZO from pyrochlore to defect-fluorite, which would precede significant He accumulation in a waste-form. The pyrochlore to defect-fluorite phase transformation may also affect the He mobility; Wiss et al. [12] measured a higher He retention capacity in defect-fluorite than in pyrochlore GZO. Samples were implanted to various He fluences corresponding to the expected He concentration at different timescales in a GZO waste-form. Bubble formation and morphology were examined using transmission electron microscopy (TEM). Lattice parameter changes resulting from irradiation damage and He accumulation were measured using grazing incidence x-ray diffraction (GIXRD).

2. Experimental methods

2.1. Sample preparation

Two sets of polycrystalline GZO samples were used in this work. Set #1 samples (5 × 10 mm), which were prepared by the sol-gel routine and sintered in a hot isotactic press as described in Nachimuthu et al. [13], were approximately 97% of the theoretical density. Set #2 samples (10 mm in diameter) were prepared by conventional solid-state synthesis. ZrO_2 and Gd_2O_3 powders were mixed in stoichiometric ratios, ball milled for 18 h, pressing the powders into pellets using a room temperature uniaxial press, and sintering in air at 1100 °C for 48 h. The powder was then ball milled again for 12 h, pressed at room temperature, and sintered in air at 1300 °C for 48 h. Finally, the powder was ball milled for 12 h, pressed into thin pellets and sintered at 1600 °C for 72 h to form the ordered pyrochlore phase. GZO samples were 95% of the theoretical

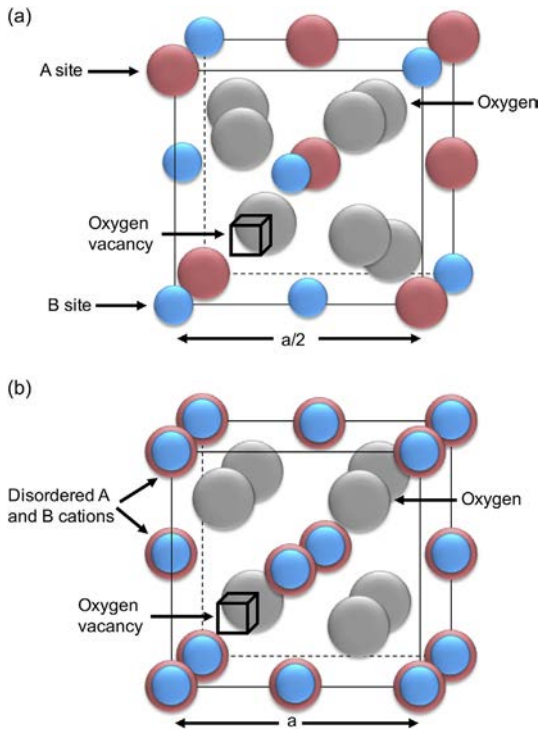

Fig. 1. Schematic showing the differences between the (a) pyrochlore structure, where cations and oxygen vacancies are ordered, and (b) defect-fluorite, where, in addition to oxygen vacancy disorder, cations are randomly arranged on the A- and B-sites. $Gd_2Zr_2O_7$ undergoes an order-disorder transformation from pyrochlore to defect-fluorite under irradiation.

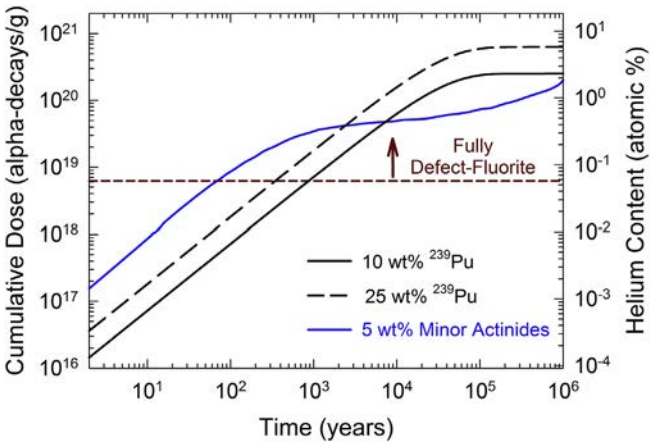

Fig. 2. Dose and He accumulation in $Gd_2Zr_2O_7$ as a function of geological time for various waste loadings. $Gd_2Zr_2O_7$ will be fully transformed to the defect-fluorite structure above the dotted line.

density as measured by Archimedes method. The as-synthesized samples were polished using diamond lapping film down to 1 μm and finished using 0.02 μm colloidal silica solution to remove residual polishing damage. Powder x-ray diffraction (XRD) patterns were recorded for both sets of samples using a PANalytical Empyrean x-ray diffractometer equipped with a Cu Kα x-ray tube, a fixed flat plate powder sample stage, 0.02 rad Soller slits, 1/8th divergence slit, 1/4th anti-scatter slits, a 10 mm mask, a Ni filter, and a PIXcel detector. Theoretical densities, lattice parameters and crystallite sizes were determined using the General Structure Analysis System (GSAS) for Rietveld refinement of powder XRD patterns [14,15]. Since the r_A/r_B of $Gd_2Zr_2O_7$ resides at the borderline of the phase stability between pyrochlore and defect-fluorite, the Gd and Zr atomic occupancy were refined due to the possibility of slight atomic disorder in the pyrochlore structure. The measured lattice parameter was 10.5318(1) Å for the Set #1 and 10.52515(6) Å for the Set #2 samples. Crystallite sizes were determined using the isotropic Lorentzian broadening due to the crystallite size term, LX, in GSAS, and were found to be similar for both sets of samples. The measured crystallite size was 208.76 nm for the Set #1 and 227.68 nm for the Set #2 samples.

2.2. Irradiations

Au irradiations were performed at the University of Tennessee's Ion Beam Materials Laboratory [16] using the 3.0 MV Pelletron tandem accelerator, and He implantations were performed at Los Alamos National Laboratory's Ion Beam Materials Laboratory using the 200 kV Danfysik Research Implanter. The irradiations were performed in 5×10^{-5} Pa vacuum with the ion beam oriented normal to the sample surface. In order to simulate α-recoil damage and induce the pyrochlore to defect-fluorite phase transformation, all samples were pre-damaged with 7 MeV Au^{3+} to a total fluence of 2.2×10^{15} Au/cm^2, which corresponds to damage accumulation over several thousand years in a waste-form containing 25 wt% ^{239}Pu (Fig. 2). During the Au irradiation, the ion flux was kept constant (8.1×10^{11} ions/cm^2/s) and the ion beam was rastered over the irradiated area of 10 × 10 mm to ensure a uniform irradiation (at scanning frequencies of 517 and 64 Hz for the horizontal and vertical directions, respectively, and a current density of 3.89 nA/mm^2). A glass scintillator and a CCD camera were used to accurately locate the ion beam. The room temperature Au irradiations produced a beam heating of ~50 °C, as measured by a K-type (chromel-alumel) thermocouple at the sample surface.

Set #1 samples were implanted with 200 keV He^+ at 2×10^{15} and 2×10^{16} He/cm^2, corresponding to 0.1 and 1.0 at. % He, respectively, to observe swelling and search for evidence of He bubble nucleation during the first million years of waste-form storage. Since He bubbles did not form at 1.0 at.% He, a third sample (Set #2) was implanted with a higher fluence to see if bubbles would form in GZO at very high doses. This Set #2 sample was implanted with 65 keV He^+ at 2×10^{17} He/cm^2, which corresponds to 12 at.% He at the peak. This sample was implanted at 65 keV to move the He peak closer to the surface, which enables easier TEM sample preparation of an already porous sample expected to contain a large quantity of bubbles that might induce cracking. For the GIXRD study, the Set #1 samples implanted with 200 keV He^+ to 2×10^{15} and 2×10^{16} He/cm^2 and a Set #2 sample implanted with 200 keV He^+ to 2×10^{17} He/cm^2 (10 at.% He at the peak, see Fig. 3(c)) were utilized. The 200 keV He^+ implants were done using a flux of 1.1×10^{13} He/cm^2/s for the 2×10^{15} and 2×10^{16} He/cm^2 irradiations, and 2×10^{13} He/cm^2/s for the 2×10^{17} He/cm^2 irradiation. The 65 keV He^+ implantation was done using a flux of 7.39×10^{12} He/cm^2/s. The beam heating was less than 35 °C during the He implantations where active air cooling was applied to the sample stage. Damage dose and He concentration values were simulated using full cascade calculations in the Stopping and Range of Ions in Matter (SRIM) code [17], using 2008 stopping powers, with all displacement energies set to 50 eV [4], and theoretical density, and are shown in Fig. 3. The experiment was designed such that Au concentration peak was deeper than the He profile peak, preserving the chemical integrity of GZO at the region of interest (the Au concentration is low, only 0.06 at.% at the peak). The peak Au dose was ~8 dpa, while the He dpa and concentration increase with He fluence. In the case of the 0.1 at.% He sample, the peak He dose was 0.035 dpa (200 keV implant), but significantly increased to 4.5 dpa at 12 at.% He (65 keV implant).

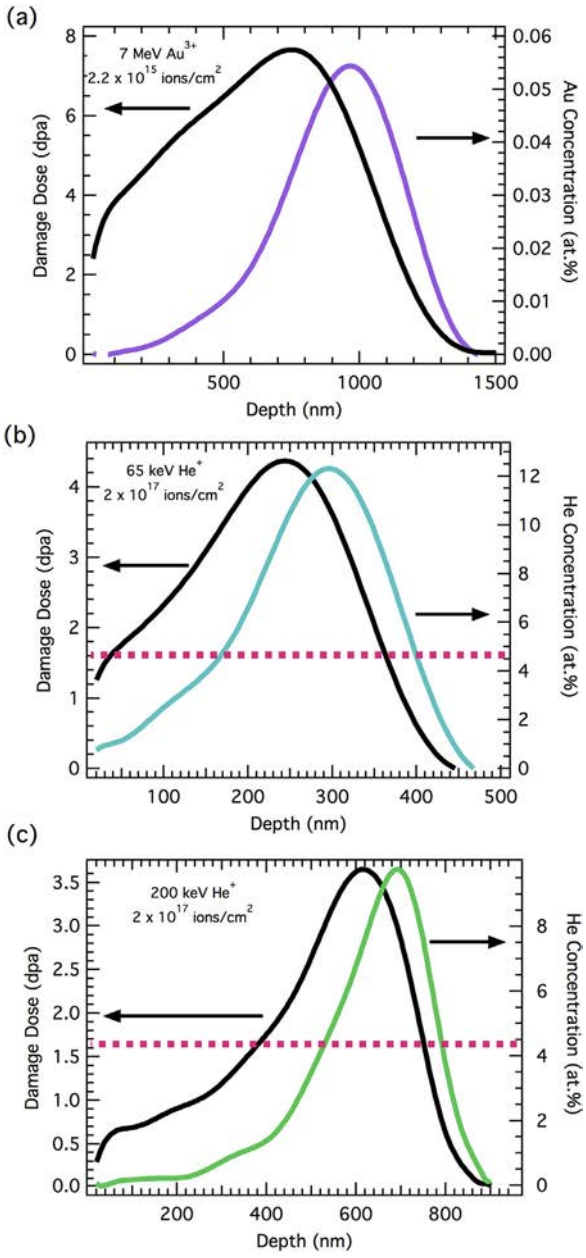

Fig. 3. SRIM calculated damage (dpa) and ion concentration profiles for $Gd_2Zr_2O_7$ (a) pre-damaged with 7 MeV Au^{3+} to 2.2×10^{15} Au/cm^2, (b) implanted with 65 keV He^+ to 2×10^{17} He/cm^2, and (c) implanted with 200 keV He^+ to 2×10^{17} He/cm^2 (2×10^{16} and 2×10^{15} He/cm^2 profiles are one and two orders of magnitude less, respectively). Dashed line indicates the He concentration at which bubbles were first observed (4.6 at.%) to aid the reader in comparing the nucleation depths for each 2×10^{17} He/cm^2 irradiation.

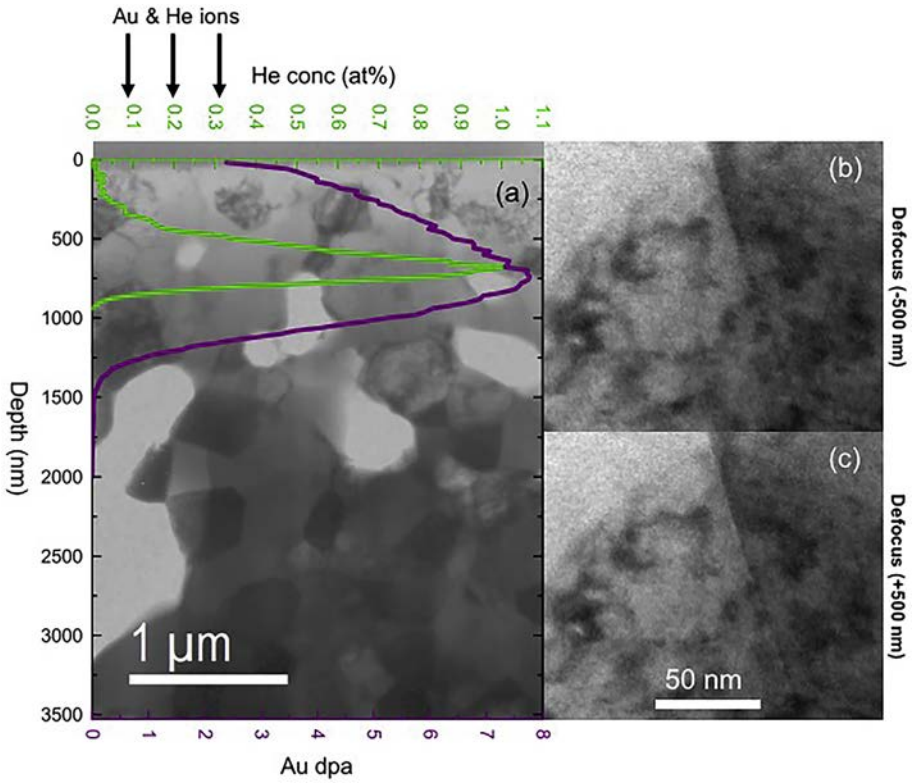

Fig. 4. TEM images obtained from the $Gd_2Zr_2O_7$ sample irradiated with 7 MeV Au^{3+} to 2.2×10^{15} Au/cm^2 and then implanted with 200 keV He^+ to 2×10^{16} He/cm^2 (1 at.% at He peak). He concentration and Au damage distribution ranges as determined by SRIM are compared to the overview image in (a). After imaging several locations near the He peak, no bubbles were observed in this sample. An example region on a grain boundary, where bubbles were expected to first nucleate, is shown at (b) −500 nm underfocus and (c) +500 nm overfocus.

2.3. Characterization

The critical He concentration required for bubble formation, as well as details about bubble morphology, were determined using TEM. TEM samples 50–150 nm in thickness were prepared using an FEI Nova 200 Nanolab Dual Beam focused ion beam (FIB). The sample surface was protected from subsequent ion beam damage from the FIB by first depositing a thin layer (<500 nm) of Pt square over a 20 × 20 μm area using a 5 keV electron beam. A 20 × 3 × 3.5 μm Pt rectangular bar was then deposited over this square using a 30 kV ion beam with varying currents from 90 pA to 0.20 nA (varying Pt density from high to low). Focused ion beam milling was then performed at 30 kV and 93 pA, followed by a final clean using a 5 kV Ga beam with current of 12 pA to remove redeposited material on the surface during the milling process, and to remove residual milling damage. TEM imaging was performed at the National Renewable Energy Laboratory (NREL) using an FEI Tecnai operating at 300 kV in TEM mode. Images were collected using a Gatan Osiris CCD camera. Samples were observed using a 10–60 μm objective aperture, depending on sample thickness. Helium bubbles were imaged using the through-focusing technique, in which Fresnel contrast produces a white spot with a dark outer ring in the underfocused condition and a dark spot with a white ring at the same location in overfocused condition. The image was initially focused by expanding the Fourier transform to the largest possible diameter, then defocused in series from −1.5 to +1.5 μm at the SRIM predicted He peak location to confirm the presence or absence of He bubbles. Defocus values may vary by an estimated ±100 nm due to error in finding the zero (focused) point. TEM images were noise filtered in Gatan Inc.'s Digital Micrograph™ and brightness and contrast were adjusted to improve clarity. Helium bubbles were quantified using the 'Analyze Particle' feature in ImageJ [18]. ImageJ provides the cross-sectional area of each bubble in nanometers, which was then converted to bubble radius using a circular cross-sectional area approximation. Since some bubbles formed chains, the circular approximation is not true in all cases.

A pristine (Set #2) pyrochlore, a Au irradiated defect-fluorite sample (Set #2), samples implanted with 200 keV He^+ to 2×10^{15} and 2×10^{16} He/cm^2 (Set #1) and to 2×10^{17} He/cm^2 (Set #2) were measured using GIXRD. All GIXRD measurements were done using a PANalytical X'Pert^3 X-ray diffractometer equipped with a 1/16th divergence slit, a parallel beam mirror, 0.02 rad Soller slits and a 4 mm mask on the incident beam side, and a 0.09 parallel plate collimator, 0.02 rad Soller slits and a Xe gas proportional detector on the diffracted side. X-ray penetration depths were calculated based on total external reflection theory using bulk density values [19,20]. A plot of the X-ray penetration depth as a function of grazing angle is provided in the supplemental file. Peak positions (in degrees 2θ) were obtained by fitting with a pseudo-voigt function using the software CMPR [21] and were converted to lattice parameters using Bragg's law. Lattice parameter and volume swelling errors were propagated from the standard deviation provided by the fit in CMPR.

3. Results and discussion

An overview image showing the entire irradiated region for the GZO sample pre-damaged and implanted with 200 keV He^+ to 2×10^{16} He/cm^2 is shown in Fig. 4(a). Fig. 4(b) and (c) show under- and overfocused images, respectively, at a grain boundary near the He concentration peak, where bubbles would be expected to first

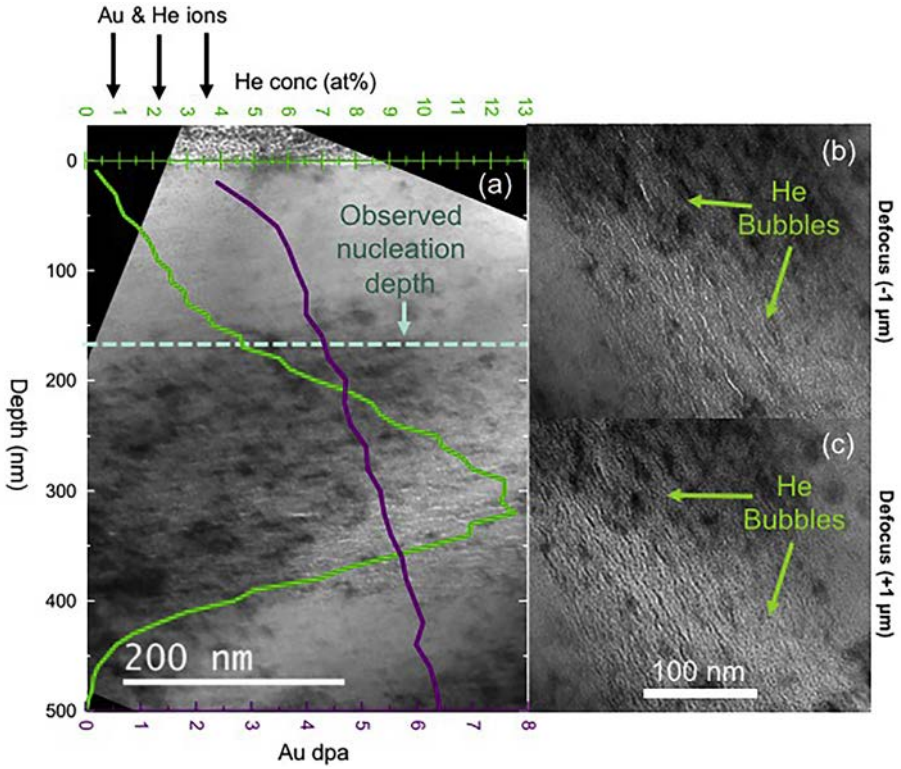

Fig. 5. TEM images for the $Gd_2Zr_2O_7$ sample irradiated with 7 MeV Au^{3+} to 2.2 × 10^{15} Au/cm^2 and then implanted with 65 keV He^+ to 2 × 10^{17} He/cm^2 (12.7 at.% He at peak). He concentration and Au damage distribution ranges as determined by SRIM are compared to the overview image in (a). Images obtained at defocus values of ±1 μm are shown for (b) underfocus and (c) overfocus conditions. Helium bubbles clearly formed at the expected He peak location, in some cases forming chains 10–30 nm in length. Bubbles were observed to nucleate starting at a depth of 165 nm (dashed line), which corresponds to 4.6 at.% He in the SRIM calculated concentration profile.

nucleate. As exemplified in Fig. 4(b) and (c), no He bubbles were observed in the pre-damaged sample implanted with 2 × 10^{16} He/cm^2. It is therefore reasonable to conclude that bubbles are not present in the sample implanted with 200 keV He^+ to a lower fluence of 2 × 10^{15} He/cm^2. Fig. 5(a) shows an overview of the He implanted region of the sample implanted with 65 keV He^+ to 2 × 10^{17} He/cm^2. Fig. 5(b) and (c) clearly show He bubbles in the under- and overfocused images, respectively, at the He concentration peak. Individual bubbles were observed starting at ~165 nm from the surface, which corresponds to a concentration of 4.6 at.% He based on the SRIM calculated He concentration profile (Fig. 5(a)). Bubbles were 1–3 nm in diameter (Fig. 6) and many formed chains 10–30 nm in length parallel to the surface.

Helium bubbles chains have been observed in other ceramics, including yttria-stabilized zirconia (YSZ) [22,23], 4H–SiC [24], MAX phase [25], and $LiNbO_3$ [26]. Ofan et al. [26] summarized the physics governing He bubble sizes and spatial distributions in He irradiated materials, and concluded that the strain distribution can cause bubbles to arrange themselves in a pseudoperiodic order to reduce the strain field in the lattice. Helium bubbles were observed in yttria-stabilized zirconia (YSZ), which also assumes the defect-fluorite crystal structure, at the same fluence, 2 × 10^{17} He/cm^2, and were also observed to form chains parallel to the surface in both single and polycrystalline samples [22,23]. Yang et al. [23] studied the effect of He irradiation on strain as a function of depth in He implanted YSZ single crystals by utilizing high resolution x-ray diffraction (HRXRD). At 1 × 10^{16} He/cm^2, point defect formation produced strain normal to the surface. At a higher fluence of 8 × 10^{16} He/cm^2, additional damage resulted in a larger strain normal to the surface. In the sample irradiated with 2 × 10^{17} He/cm^2, the fluence at which He bubbles and bubble chains formed, Yang et al. measured an almost complete elimination of strain normal to the surface.

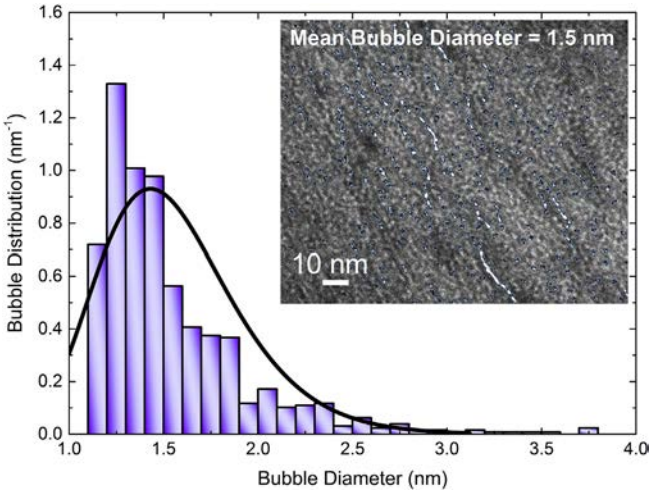

Fig. 6. Helium bubble size distribution in $Gd_2Zr_2O_7$ pre-damaged with 7 MeV Au^{3+} to a fluence of 2.2 × 10^{15} Au/cm^2 and implanted with 65 keV He^+ to 2 × 10^{17} He/cm^2, which corresponds to a peak He concentration of 12.7 at.%. Bubbles formed chains several nm in length. Bubble diameters were calculated assuming a circular cross-sectional area, which largely approximates the shape of bubbles which formed chains. Chains of bubbles have the largest cross-sectional area and therefore the largest calculated diameters. An average bubble diameter of 1.5 ± 0.2 nm was determined by fitting with a log-normal distribution (shown), with the error estimated from the TEM image pixel size (0.15 nm). Inset shows outline of areas that ImageJ used to calculate the cross-sectional bubble area during image analysis, overlaid with the original underfocused TEM image shown in Fig. 5(b).

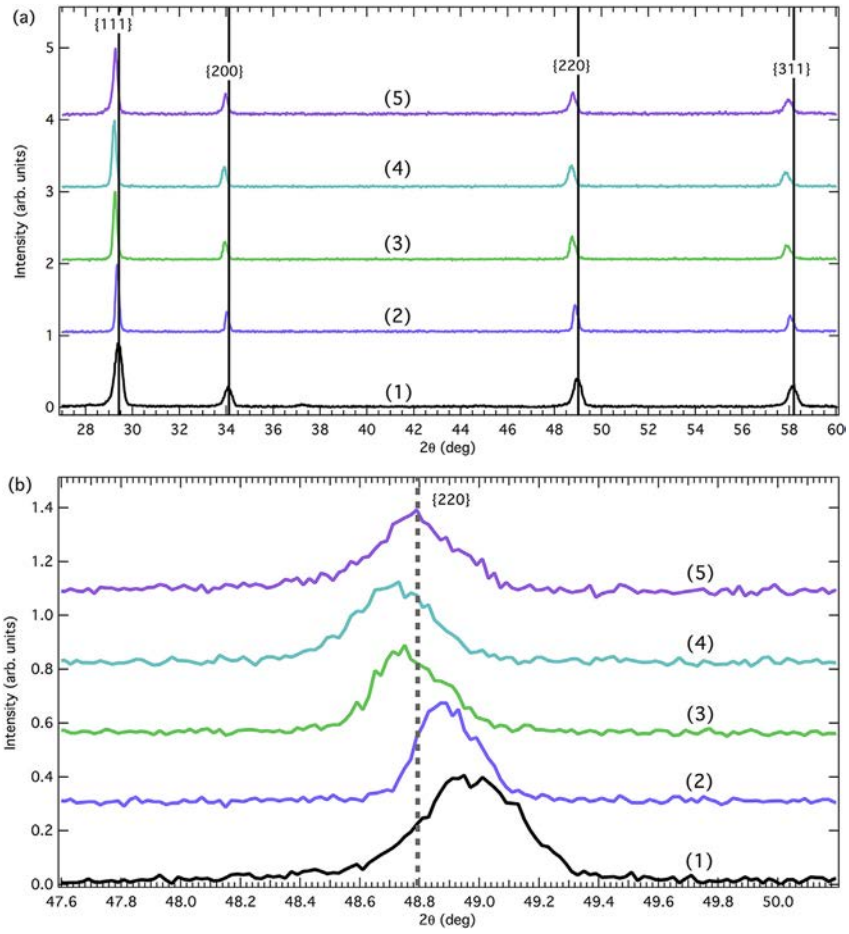

Fig. 7. (a) GIXRD patterns obtained at an incident angle of $\omega = 6^{\circ}$ (x-ray penetration depth of ~600 nm) from $Gd_2Zr_2O_7$ samples (from bottom to top): (1) pristine (unirradiated) $Gd_2Zr_2O_7$, (2) $Gd_2Zr_2O_7$ pre-damaged with 7 MeV Au^{3+} to 2.2×10^{15} Au/cm^2, and $Gd_2Zr_2O_7$ pre-damaged then 200 keV He^+ implanted to fluences of (3) 2×10^{15}, (4) 2×10^{16}, and (5) 2×10^{17} He/cm^2. (b) A zoomed view of the {220} reflection shows a clear peak shift between each of the irradiation conditions, with a dotted line indicating the center position of the highest He fluence measured. Reflections are labeled with fluorite Miller indices.

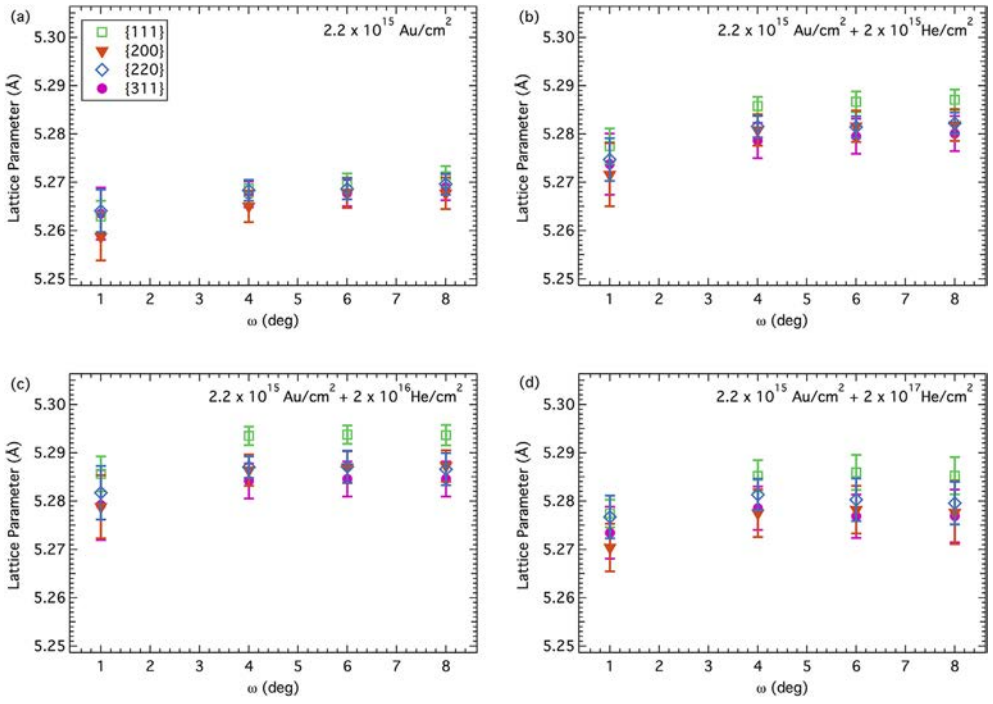

Fig. 8. Lattice parameters were calculated from the GIXRD data using the four highest intensity fluorite reflections for each grazing angle. Lattice parameters varied more between the different reflections in the He implanted samples (b–d) than in the Au irradiated sample (a), with the largest variation occurring in the sample implanted with 2×10^{16} He/cm^2 (c). Error bars represent the fractional error.

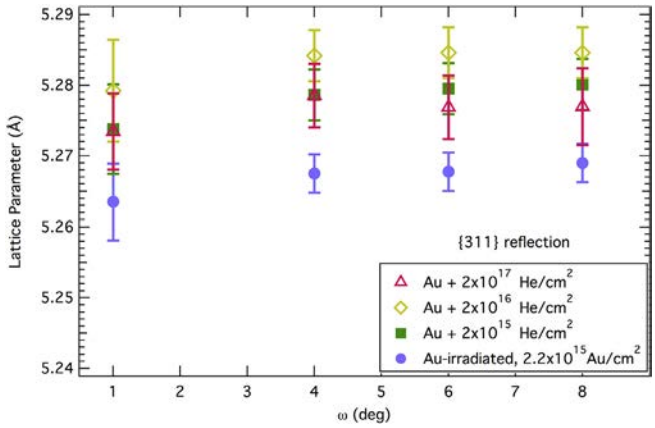

Fig. 9. Experimentally determined lattice parameters for $Gd_2Zr_2O_7$ samples implanted with 200 keV He^+ relative to the pre-damaged (Au irradiated) sample for various incident x-ray angles. Lattice parameters were calculated using the fluorite {311} reflection. Error bars represent the fractional error.

Due to the difficulty of obtaining high quality GZO single crystals for performing HRXRD measurements, polycrystalline GZO samples were implanted with 200 keV He^+ to 2×10^{15}, 2×10^{16}, and 2×10^{17} He/cm^2. Lattice parameter changes were measured using GIXRD to determine the effect of pre-damage, He irradiation damage, and He bubble chain formation on the strain in GZO. GIXRD differs from HRXRD in that data collected at each grazing angle are representative of all material up to the x-ray penetration depth; the strain cannot be explicitly determined at specific depths within the irradiated layer. Samples were measured at four grazing angles, $\omega = 1, 4, 6$, and 8°, which correspond to ~100, 400, 600, and 800 nm x-ray penetration depths, respectively. Fig. 3(b) and (c) show a SRIM profile comparison between the 65 keV He^+ implanted GZO to a fluence of 2×10^{17} He/cm^2, utilized for TEM observations, and the 200 keV He^+ implantation to the same fluence, utilized for GIXRD measurements. The dashed line in Fig. 3(b) and (c) represents the critical He concentration required for visible bubbles, 4.6 at.%, as determined in the TEM images. The four highest intensity fluorite reflections, {111}, {200}, {220}, and {311}, which were utilized for lattice parameter calculations, are shown for each irradiation condition in Fig. 7(a). A clear peak shift was observed for each irradiation condition, as shown in the zoomed {220} reflection in Fig. 7(b). Pre-damage, which converts the GZO lattice from pyrochlore to defect-fluorite, caused a shift to lower 2θ, indicating a lattice expansion. Further shifts to lower 2θ were observed for the lower fluence He irradiations at 2×10^{15} and 2×10^{16} He/cm^2. A shift to higher 2θ, however, was observed for the sample irradiated with 200 keV He^+ to 2×10^{17} He/cm^2, the fluence at which He bubbles and bubble chains were observed. Peak positions were converted to lattice parameters for each reflection and grazing angle and are compiled in Fig. 8. Errors were propagated from the fit of each peak. The lattice parameters calculated for each reflection are more similar in the pre-damaged sample than in the He irradiated samples.

Fig. 9 shows a comparison of lattice parameters calculated for each irradiation condition using only the {311} reflection. General trends were identified, even though the He implanted lattice parameter remains unchanged within error. The lattice parameter increased at each grazing angle between the pre-damaged sample and the samples implanted with 200 keV He^+ to fluences of 2×10^{15} and 2×10^{16} He/cm^2, with the 2×10^{16} He/cm^2 sample having the largest lattice parameter. In the sample implanted with 200 keV He^+ to a fluence of 2×10^{17} He/cm^2, the lattice parameter decreased to approximately the 2×10^{15} He/cm^2 value for $\omega = 1°$ and 4°, and even below the 2×10^{15} He/cm^2 value for $\omega = 6°$ and 8°. A reduction in the lattice parameter occurred for all reflections (Fig. 8(d)) after He implantation to 2×10^{17} He/cm^2. Table 1 shows a comparison of the lattice parameter, change in lattice parameter (Δa), unit cell volume, and change in unit cell volume (ΔV) for each irradiation condition, as calculated using the {311} reflection by averaging over all incident angles. Changes in lattice parameter (Δa) and unit cell volume (ΔV) were calculated independently for each grazing angle, with respect to the defect-fluorite a and V values, then averaged over all grazing angles.

We suspect the experimentally determined decrease in unit cell swelling after implantation with 200 keV He^+ to 2×10^{17} He/cm^2 is due to the formation of the He bubble chains that were observed at this fluence, as has been shown to occur in the other ceramics as discussed above. The fact that bubbles may be forming chains to reduce the total strain is significant, because this suggests that the observed bubble chain microstructure is an artifact of irradiating with ion beams, which typically produce a strain profile normal to the surface [27,28]. In a real waste form, the radiation damage would occur in random directions, which will produce a non-uniform strain profile, making it more difficult for bubbles to arrange themselves in ways that reduce the total strain. For this reason, the bubble microstructure could differ in a GZO waste-form containing the same He concentration.

4. Conclusion

This work experimentally determined the critical He concentration (4.6 at.%) required to nucleate bubbles > 1 nm in diameter in bulk $Gd_2Zr_2O_7$. Pyrochlores have been widely studied for waste immobilization purposes, but mostly with respect to radiation damage effects. Little is known about the effects of He accumulation on the GZO lattice. Bubbles were observed as both (1) individual spheres within the matrix, and (2) as chains of bubbles 10–30 nm in length parallel to the sample surface. Grazing incidence x-ray diffraction was used to experimentally examine lattice parameter changes for various irradiation conditions. Lattice swelling was found to occur as a result of irradiation with 7 MeV Au^{3+} to a fluence of 2.2×10^{15} Au/cm^2, and after irradiation with 2.2×10^{15} Au/cm^2 + 2×10^{15} He/cm^2 (200 keV) and 2.2×10^{15} Au/cm^2 + 2×10^{16} He/cm^2 (200 keV). A reduction in lattice swelling

Table 1
Experimental results from lattice swelling (Δa and ΔV). Lattice swelling in the pre-damaged (Au irradiated) sample was calculated relative to the half the lattice parameter of pristine sample. Swelling in 200 keV He^+ implanted samples was calculated relative to the pre-damaged sample (all He implanted samples were first pre-damaged). Swelling results were calculated using the fluorite {311} peak by averaging over all incident x-ray angles. Peak He concentrations were determined using SRIM.

Sample	Fluence (ions/cm^2)	Peak He at.%	a (Å)	Δa (Å)	V (Å^3)	ΔV (Å^3)
Pristine			10.527(2)		1166.6(7)	
Au Irradiated	2.2×10^{15}		5.2668(7)	0.0036(15)	146.09(6)	0.30(13)
Au + He	2×10^{15}	0.1	5.2784(12)	0.0112(3)	147.07(10)	0.94(2)
Au + He	2×10^{16}	1	5.2834(10)	0.0162(3)	147.48(9)	1.35(2)
Au + He	2×10^{17}	10	5.2768(10)	0.0099(8)	146.93(8)	0.83(7)

was measured after irradiation with 2.2×10^{15} Au/cm^2 + 2×10^{17} He/cm^2 (200 keV), the fluence at which individual bubbles and bubble chains were first observed in TEM. Thus, bubble chains are thought to form in order to reduce the lattice strain produced by damage occurring during the Au and He irradiations.

Acknowledgements

First, the authors would like to thank Kurt Sickafus for helpful discussions and use of his laboratory facilities. Helium implantations were performed at the Center for Integrated Nanotechnologies, an Office of Science User Facility operated for the U.S. Department of Energy (DOE) Office of Science by Los Alamos National Laboratory (Contract DE-AC52-06NA25396) and Sandia National Laboratories (Contract DE-AC04-94AL85000). This research was also in part supported by the National Renewable Energy Laboratory, where part of the transmission electron microscopy work was performed, which is sponsored by U.S. Department of Energy. Some initial electron microscopy was conducted as part of a user proposal at Oak Ridge National Laboratory's Center for Nanophase Materials Sciences, which is a Department of Energy Office of Science User Facility. X-ray diffraction experiments were performed using the instruments that were procured through the general infrastructure grant of DOE-Nuclear Energy University Program (DE-NE0000693). This work was supported by the Nuclear Engineering University Program (NEUP) Award Number 12-3528.

Appendix A. Supplementary data

Supplementary data related to this article can be found at http://dx.doi.org/10.1016/j.actamat.2016.05.045.

References

[1] W.J. Weber, R.C. Ewing, C.R.A. Catlow, T.D. De La Rubia, L.W. Hobbs, C. Kinoshita, H. Matzke, A.T. Motta, M. Nastasi, E.K.H. Salje, Radiation effects in crystalline ceramics for the immobilization of high-level nuclear waste and plutonium, J. Mater. Res. 13 (1998) 1434–1484.
[2] R.C. Ewing, W.J. Weber, F.W. Clinard, Radiation effects in nuclear waste forms for high-level radioactive waste, Prog. Nucl. Energy 29 (1995) 63–127.
[3] W.E. Lee, M.I. Ojovan, M.C. Stennett, N.C. Hyatt, Immobilisation of radioactive waste in glasses, glass composite materials and ceramics, Adv. Appl. Ceram. Struct. Funct. Bioceram. 105 (2006) 3–12.
[4] R.C. Ewing, W.J. Weber, J. Lian, Nuclear waste disposal—pyrochlore ($A_2B_2O_7$): nuclear waste form for the immobilization of plutonium and "minor" actinides, J. Appl. Phys. 95 (2004) 5949–5971.
[5] M.A. Subramanian, G. Aravamudan, G.V.S. Rao, Oxide pyrochlores—a review, Prog. Solid State Chem. 15 (1983) 55–143.
[6] S.-X. Wang, B.D. Begg, L.-M. Wang, R.C. Ewing, W.J. Weber, K.V. Kutty, Radiation stability of gadolinium zirconate: a waste form for plutonium disposition, J. Mater. Res. 14 (1999) 4470–4473.
[7] K.E. Sickafus, L. Minervini, R.W. Grimes, J.A. Valdez, M. Ishimaru, F. Li, K.J. McClellan, T. Hartmann, Radiation tolerance of complex oxides, Science 289 (2000) 748–751.
[8] N.P. Laverov, S.V. Yudintsev, V.I. Velichkin, A.N. Lukinykh, S.V. Tomilin, A.A. Lizin, S.V. Stefanovskii, Effect of amorphization on isolation properties of actinide pyrochlore matrix, Radiochemistry 51 (2009) 529–536.
[9] W.J. Weber, J.W. Wald, H. Matzke, Self-radiation damage in $Gd_2Ti_2O_7$, Mater. Lett. 3 (1985) 173–180.
[10] J. Lian, X.T. Zu, K.V.G. Kutty, J. Chen, L.M. Wang, R.C. Ewing, Ion-irradiation-induced amorphization of $La_2Zr_2O_7$ pyrochlore, Phys. Rev. B 66 (2002) 054108.
[11] W.J. Weber, A. Navrotsky, S. Stefanovsky, E.R. Vance, E. Vernaz, Materials science of high-level nuclear waste immobilization, MRS Bull. 34 (2009) 46–53.
[12] T.A.G. Wiss, J.P. Hiernaut, P.M.G. Damen, S. Lutique, R. Fromknecht, W.J. Weber, Helium behaviour in waste conditioning matrices during thermal annealing, J. Nucl. Mater. 352 (2006) 202–208.
[13] P. Nachimuthu, S. Thevuthasan, V. Shutthanandan, E.M. Adams, W.J. Weber, B.D. Begg, D.K. Shuh, D.W. Lindle, E.M. Gullikson, R.C. Perera, Near-edge x-ray absorption fine structure study of ion-beam-induced phase transformation in $Gd_2(Ti_{1-y}Zr_y)_2O_7$, J. Appl. Phys. 97 (2005) 033518.
[14] A.C. Larson, R.B. Von Dreele, General Structure Analysis System (GSAS), 2000, pp. 86–748. Los Alamos National Laboratory Report LAUR.
[15] B.H. Toby, EXPGUI, a graphical user interface for GSAS, J. Appl. Crystallogr. 34 (2001) 210–213.
[16] Y. Zhang, M.L. Crespillo, H. Xue, K. Jin, C.H. Chen, C.L. Fontana, J.T. Graham, W.J. Weber, New ion beam materials laboratory for materials modification and irradiation effects research, Nucl. Instrum. Methods Phys. Res. Sect. B Beam Interact. Mater. Atoms 338 (2014) 19–30.
[17] J.F. Ziegler, J.P. Biersack, U. Littmark, The Stopping Range of Ions in Solids, 1985.
[18] W.S. Rasband, ImageJ, U.S. National Institutes of Health, Bethesda, Maryland, USA, http://imagej.nih.gov/ij/.
[19] M.F. Toney, T.C. Huang, S. Brennan, Z. Rek, X-ray depth profiling of iron oxide thin films, J. Mater. Res. 3 (2011) 351–356.
[20] G. Renaud, Oxide surfaces and metal/oxide interfaces studied by grazing incidence X-ray scattering, Surf. Sci. Rep. 32 (1998) 5–90.
[21] B.H. Toby, CMPR – a powder diffraction toolkit, J. Appl. Crystallogr. 38 (2005) 1040–1041.
[22] T. Yang, C.A. Taylor, C. Wang, Y. Zhang, W.J. Weber, J. Xiao, J. Xue, S. Yan, Y. Wang, Effects of He irradiation on yttria-stabilized zirconia ceramics, J. Am. Ceram. Soc. 98 (2015) 1314–1322.
[23] T.H. Yang, X. Huang, Y. Gao, C. Wang, Y. Zhang, J. Xue, S. Yan, Y. Wang, Damage evolution of yttria-stabilized zirconia induced by He irradiation, J. Nucl. Mater. 420 (2012) 430–436.
[24] C.H.D. Zhang, S.E. Vishnyakov, V.M. Evans, J.H. Evans, Dose dependence of formation of nanoscale cavities in helium-implanted 4H–SiC, J. Appl. Phys. 94 (2003) 6017–6022.
[25] C.Y. Wang, T. Yang, S. Kong, J. Xiao, J. Xue, Q. Wang, C. Hu, Q. Huang, Y. Wang, Effects of He irradiation on Ti_3AlC_2: damage evolution and behavior of He bubbles, J. Nucl. Mater. 440 (2013) 606–611.
[26] A. Ofan, L. Zhang, O. Gaathon, S. Bakhru, H. Bakhru, Y. Zhu, D. Welch, R. Osgood, Spherical solid He nanometer bubbles in an anisotropic complex oxide, Phys. Rev. B 82 (2010) 104113.
[27] A. Debelle, A. Declémy, XRD investigation of the strain/stress state of ion-irradiated crystals, Nucl. Instrum. Methods Phys. Res. B 268 (2010) 1460–1465.
[28] G. Sattonnay, S. Moll, M. Herbst-Ghysel, C. Legros, J.-M. Costantini, L. Thomé, Mechanical stresses induced in ceramic oxides by ion irradiation, Nucl. Instrum. Methods Phys. Res. Sect. B Beam Interact. Mater. Atoms 266 (2008) 3052–3056.